Hindawi
Journal of Analytical Methods in Chemistry
Volume 2017, Article ID 3012364, 8 pages
https://doi.org/10.1155/2017/3012364

Research Article

Synthesis, Characterization, and Adsorptive Properties of Fe_3O_4/GO Nanocomposites for Antimony Removal

Xiuzhen Yang,[1] Tengzhi Zhou,[1] Bozhi Ren,[1] Zhou Shi,[2,3] and Andrew Hursthouse[1,4]

[1]*College of Civil Engineering, Hunan University of Science and Technology, Xiangtan 411201, China*
[2]*College of Civil Engineering, Hunan University, Changsha 410082, China*
[3]*Key Laboratory of Building Safety and Energy Efficiency, Ministry of Education, Hunan University, Changsha 410082, China*
[4]*School of Science & Sport, University of the West of Scotland, Paisley PA1 2BE, UK*

Correspondence should be addressed to Xiuzhen Yang; 8436691@qq.com

Received 28 February 2017; Revised 1 June 2017; Accepted 6 June 2017; Published 20 July 2017

Academic Editor: Ricardo Jorgensen Cassella

A magnetic Fe_3O_4/GO composite with potential for rapid solid-liquid separation through a magnetic field was synthesized using GO (graphene oxide) and Fe_3O_4 (ferriferous oxide). Characterization of Fe_3O_4/GO used scanning electron microscope (SEM), X-ray diffractometer (XRD), Fourier transform infrared spectrometer (FT-IR), and Vibrating Sample Magnetometer (VSM). A number of factors such as pH and coexisting ions on adsorbent dose were tested in a series of batch experiments. The results showed that GO and Fe_3O_4 are strongly integrated. For pH values in the range of 3.0~9.0, the removal efficiency of Sb(III) using the synthesized Fe_3O_4/GO remained high (95%). The adsorption showed good fit to a pseudo-second-order and Langmiur model, with the maximum adsorption capacity of 9.59 mg/g maintained across pH 3.0–9.0. Thermodynamic parameters revealed that the adsorption process was spontaneous and endothermic. Analysis by X-ray photoelectron spectroscopy (XPS) showed that the adsorption process is accompanied by a redox reaction.

1. Introduction

Antimony has recently gained considerable attention as a toxic heavy metal [1]. By binding with sulfhydryl groups inside human body, antimony and antimony compounds can interfere in enzyme activity or destroy intracellular ionic equilibrium which leads to cell hypoxia, causing metabolic disorders and injury to the nervous system and other organs [2].

Antimony has been classified as a priority pollutant by European Union (EU) and United States Environmental Protection Agency (EPA) in 1976 and 1979, respectively [3, 4]. The Environmental Protection Department of Japan also listed it as a pollutant of concern and stipulated a maximum acceptable concentration of 2 ug/L [5]. In China, the maximum concentration of antimony limited by GHZBl and Drinking Water Health Standards is 5 ug/L [6], which is consistent with the standards of World Health Organization [7].

China has the largest reserve and capacity for production of antimony in the world [8]. Over 80% of total world antimony production is in China in the past several decades, and use is wide spread as a catalyst in cPET production, in flame retardants, in alloys, and in the electronics industry. The main production areas are in Hunan in the southwest of China, where the 100-year-old mine, Xikuangshan, is known as the World Antimony Capital. The region has a history of nearly 200 years of antimony ore production and, therefore, antimony pollution in this region is of concern. Research shows that the antimony content of water in the mining area can exceed 7,000 ug/L [9]. The severity of antimony pollution has threatened the health of residents surrounding the mine. Therefore, cost effective methods to control antimony pollution in China, especially in the southwest, have become an imperative.

Toxicity of antimony is mainly affected by its valence state and the nature of compounds with the toxicity of trivalent antimony being ten times higher than that of pentavalent

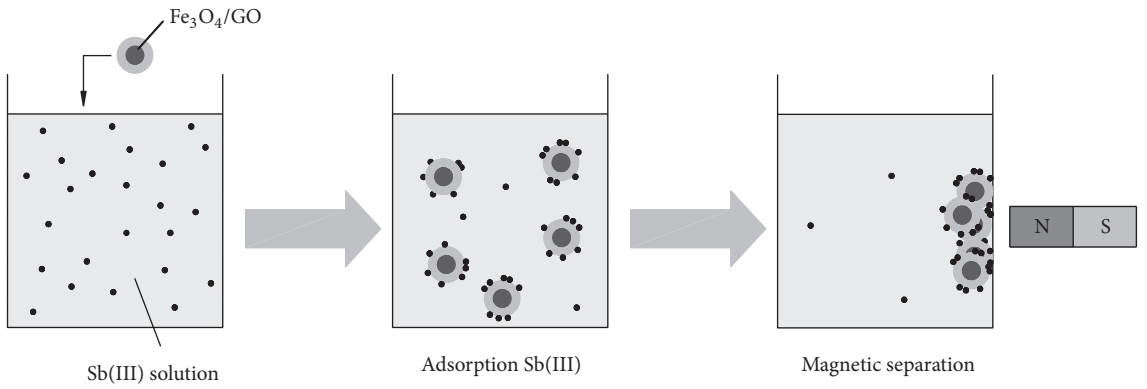

Figure 1: The adsorption experiment process.

antimony [10–12]. Hence, trivalent antimony is chosen as the target oxidation state of this pollutant.

A variety of methods have been developed to remove antimony from solution, of which approaches using adsorption are popular due to the effectiveness and availability of of reactive solid phases. Due to the huge specific surface area (2,630 m^2/g) [13], Graphene Oxide (GO) has been widely applied in water treatment; however, its strong sorption makes it difficult to desorb after reaction. The preparation of Fe_3O_4/GO nano composites for effective pollutant removal has been demonstrated [14] showing strong affinity and reversibility for a number of pollutants and was prepared in this experiment to evaluate removal of antimony from water.

2. Materials and Methods

2.1. Reagent and Instrument

Raw Material and Reagent. Graphene Oxide (prepared by modified Hummers' method) and the regents (antimony potassium tartrate, sodium hydroxide, hydrochloric acid, etc.) were analytically pure.

Key Instruments. The key instruments are Scanning electron microscope (JSM-6700F, Japan, JEOL); X-ray diffractometer (D8/ADVANCE, Germany, BRUKER); Fourier transform infrared spectrometer (IRAffinity-1, Japan Shimadzu); magnetometer (MPMS-XL-7, the United States, Quantum Design Company); atomic absorption spectrophotometer (AA-7000, Japan, JEOL).

2.2. Preparation of Fe_3O_4/GO. Fe_3O_4 particles were prepared by coprecipitation method. The successful in situ growth of Fe_3O_4 nanoparticles on GO surface during the synthetic process of Fe_3O_4/GO composites was ascribed to the oxygen-containing functional groups of GO. The as-synthesized composites in this study not only have the excellent adsorption properties of GO, but also possess the superparamagnetism of Fe_3O_4 nanoparticles. Hence, the proportion of Fe_3O_4 to GO needed optimization during the preparation of composites to take advantage of the strong adsorption properties of GO and the magnetism of Fe_3O_4.

GO (15 mg) was dispersed into DI water (30 ml) by ultrasonication for 30 min. To this suspension, 50 ml solution of $FeCl_3$ (110 mg) and $FeCl_2$ (43 mg) in DI water was added at room temperature. Then the temperature was raised to 85°C and a 30% ammonia solution was added increasing the pH to 10.0. After being rapidly stirred for 1 h the solution was cooled to room temperature. The resulting black precipitate was centrifuged at 4500 rpm for 10 min and washed three times with DI water and finally dried in a vacuum oven at 60°C for overnight to yield the Fe_3O_4/GO composite.

2.3. Adsorption Experiments. The model wastewater with varying concentration of Sb(III) was prepared using antimony potassium tartrate. Aliquots of 50 ml of model wastewater with the appropriate Sb concentration and a quantity of Fe_3O_4/GO were added. Batch adsorption experiments were undertaken at a constant temperature with shaking prior to magnetic separation of the residue. The supernatant was filtered using a 0.45 um membrane, and the concentration of residual Sb(III) in solution was measured by atomic absorption spectrophotometry. The factors influencing sorption investigated included the initial pH value, the Fe_3O_4/GO dose, adsorption time, and temperature.

The removal rate (%) was calculated from

$$\text{Removal rate} = \frac{c_0 - c_t}{c_0} \times 100\%, \quad (1)$$

where c_0 and c_t are the initial and final concentrations of Sb(III) in the solution (mg/l), respectively.

It was a static adsorption experiment, and the experimental arrangement is shown in Figure 1.

3. Result and Discussion

3.1. Solid Characterization

3.1.1. SEM. Figure 2 showed the SEM images of GO and Fe_3O_4/GO at different magnification. The SEM images (b) and (c) show the Fe_3O_4 Nps added as bright dots that were uniformly spread over the surface of the GO, which indicated that the Fe_3O_4 was coated on the GO successfully. Magnetic Fe_3O_4 nanoparticles formed in alkaline condition could be

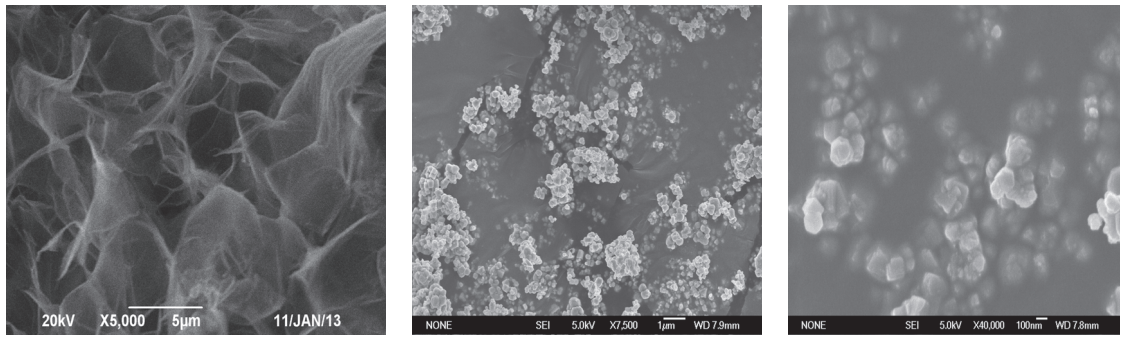

(a) (b) (c)

Figure 2: (a) SEM images of GO; (b) and (c) SEM images of Fe_3O_4/GO at different magnification.

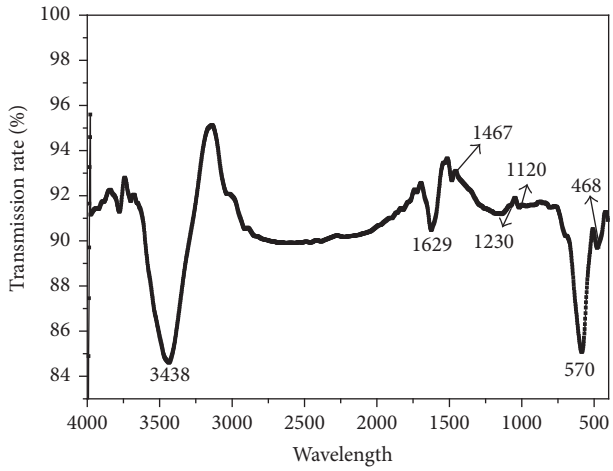

Figure 3: FT-IR patterns of Fe_3O_4/GO.

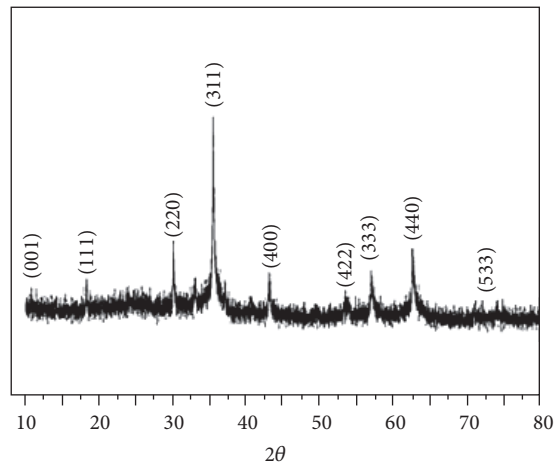

Figure 4: XRD patterns of Fe_3O_4/GO.

firmly loaded on GO because the Fe^{3+} and Fe^{2+} in solution reacted with the carboxyl functional groups of GO to form coordination compounds that were easily deposited on the surface of GO.

The reaction processes are previously identified as (2)–(4) [15].

$$2Fe^{2+} + GO \longrightarrow 2Fe^{3+} + rGO \quad (2)$$

$$Fe^{2+} + 2Fe^{3+} + 8OH^- \longrightarrow Fe_3O_4 + 4H_2O \quad (3)$$

$$3Fe^{2+} + GO\left(8OH^-\right) \longrightarrow Fe_3O_4 + 4H_2O + rGO \quad (4)$$

3.1.2. FT-IR. The images in Figure 3 show the FT-IR spectrum for Fe_3O_4/GO composites. Two strong vibration stretch peaks appeared at 570 cm^{-1} and 468 cm^{-1}, which were characteristic absorption peaks of Fe-O bond [16]. The absorption peaks at 3438 cm^{-1}, 1629 cm^{-1}, 1230 cm^{-1}, and 1120 cm^{-1} were related to the vibration peak of molecular adsorption, the vibration absorption peak of C=O in carboxyl, C=O-H or vibration of ketone skeleton, and the vibration of C-O-C, respectively [17]. The results indicated that a large amount of oxygen-containing functional groups exist on the surface of the GO and Fe_3O_4 nanocomposite.

3.1.3. XRD. The powder X-ray diffraction pattern in Figure 4 for Fe_3O_4/GO composites shows the diffraction basal spacing (001) is due to the crystalline GO (with 2θ at 10.9°). Seven distinct diffraction peaks of varying FWHM are identified for 2θ at 30.1°, 35.4°, 43.1°, 53.2°, 62.7°, and 74.0° and correspond to cubic phase crystal structure of Fe_3O_4 which were (220), (311), (400), (422), (440), and (533), respectively [18]. Moreover, it can be noted that there was no other impurity peak in XRD, which means the in situ growth of GO and Fe_3O_4 did not affect the structure of Fe_3O_4 during the synthesis of the Fe_3O_4/GO composites. The cubic structure of Fe_3O_4 is confirmed.

3.1.4. Vibrating Sample Magnetometer. The plot in Figure 5 shows the hysteresis loop of the composite adsorbent. The specific magnetism was up to 87.3 emu/g, which indicated that the composite could achieve fast solid-liquid separation under the applied magnetic field.

The hysteresis loop of Fe_3O_4/GO was close to "S," and the surplus magnetic strength and magnetic coercive force were nearly zero and thus it belongs to soft magnetism. It confirms that Fe_3O_4/GO composites were superparamagnetic. The results confirm good separation potential as reported

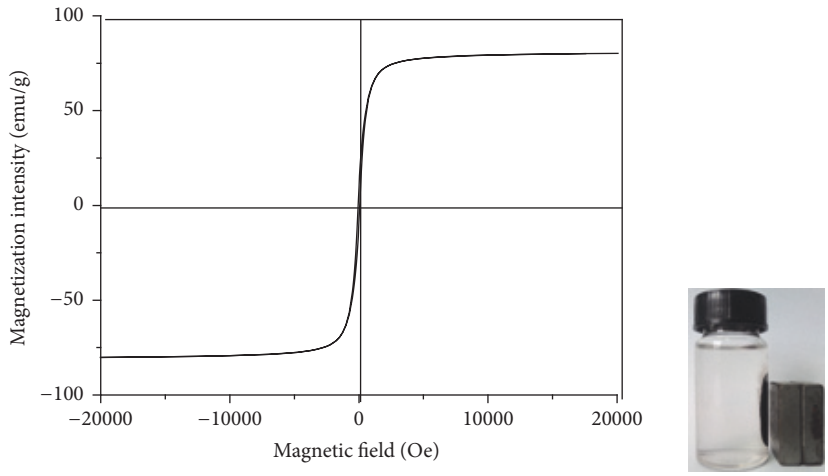

FIGURE 5: The hysteresis loop of Fe_3O_4/GO.

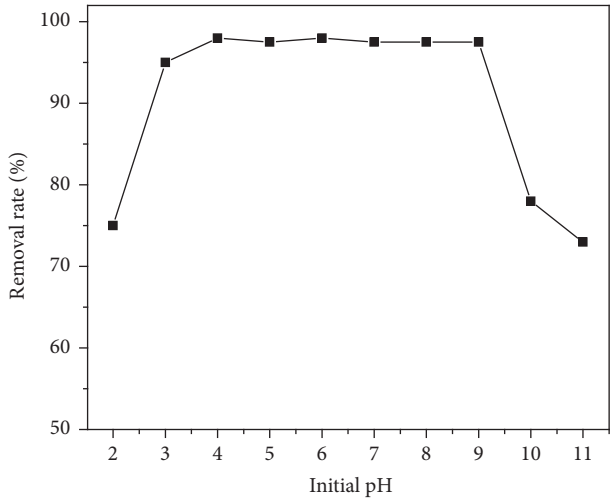

FIGURE 6: Effects of pH on adsorption efficiency of Sb(III).

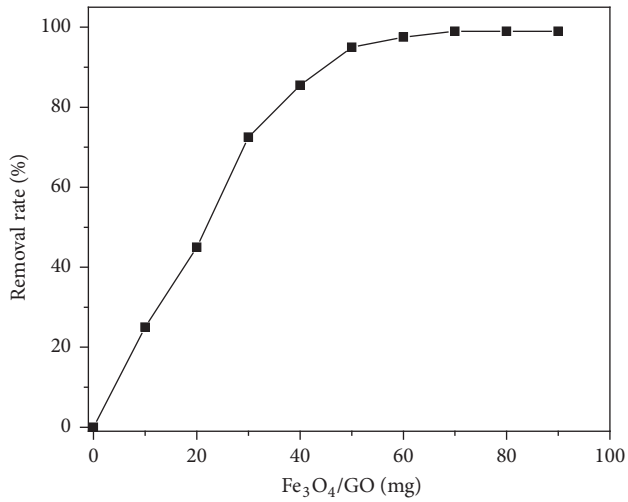

FIGURE 7: Effects of Fe_3O_4/GO dosage on removal efficiency of Sb(III).

elsewhere, and strong potential for recovery and reuse in sorption treatment systems [19].

3.2. Evaluation of the Performance of Fe_3O_4/GO Composite in the Adsorption of Sb(III)

3.2.1. The Effect of pH. An experiment on the effect of pH on Sb(III) adsorption was carried out over the pH range of 2.0–11.0. The initial concentration of antimony was C_0 = 10 mg/L; and the dose of Fe_3O_4/GO was 100 mg/50 ml; the reaction temperature was T = 298 K; reaction time was t = 120 min, with the mixing speed of 120 r/min. Experimental results are shown in Figure 6.

Figure 6 indicated that the adsorption of Sb(III) by using Fe_3O_4/GO was not affected in the pH range of 3.0–9.0, and the maximum removal rate was over 95%. This phenomenon is because the species of Sb(III) are pH dependent: when the pH is below 3.0, the predominant species of Sb(III) are SbO^+ and $Sb(OH)^{2+}$, when the pH ranges from 3.0 to 9.0 $Sb(OH)_3$ and $HSbO_2$ are the main species of Sb(III), and only SbO^{2-} exists when the pH is above 9.0 [20]. Since the highest adsorption is achieved at pH 3.0–9.0 and pH value of the aquatic environment is usually around 7.0, thus pH 7.0 is selected in further experiments.

3.2.2. Effect of Sorbent Dose. 10 × 50 ml samples of Sb(III) solution with an initial concentration of 10 mg/L were taken. The solution was added in a 100 ml polyethylene bottle, and pH was adjusted to 7.0. Finally, the solution was mixed in a constant temperature shaker (298 K) for 120 minutes.

As shown in Figure 7, adsorption removal rate of Sb(III) increased with the Fe_3O_4/GO dose. Initially, there was a sharp increase in the rate of adsorption, which later slowed down. The adsorption equilibrium was achieved at a dose of 60 mg. This might be explained by the fact that the contact area between adsorbate and adsorbent became larger and the adsorption points of Fe_3O_4/GO increased with the

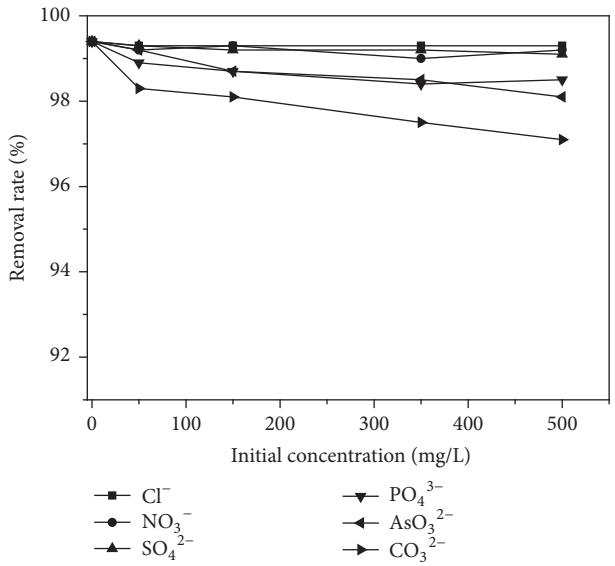

Figure 8: Effects of the coexisting ions.

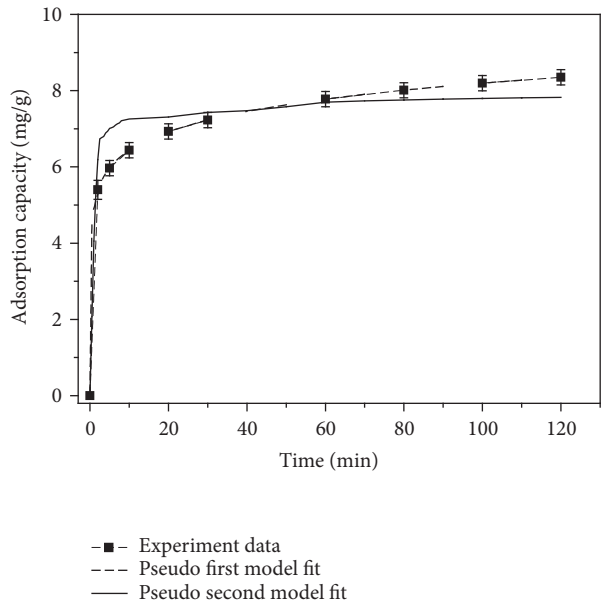

Figure 9: Kinetics models for fitting Sb(III) adsorption using Fe_3O_4/GO.

addition of Fe_3O_4/GO. Furthermore, the difference in Sb(III) concentration between initial adsorbent and adsorbate was relatively large and more Sb(III) could be adsorbed by Fe_3O_4/GO, which also leaded to a fast adsorption at the initial stage. With the increase of sorbent dose, adsorption of Sb(III) could reach up to 100%. In subsequent experiments, 60 mg/50 ml was chosen as the optimum dose.

3.2.3. Effect of Coexisting Ions. Effect of various anions on Sb(III) adsorption efficiency was investigated. A series of experiments using Cl^-, NO_3^-, SO_4^{2-}, PO_4^{3-}, AsO_3^{2-}, and CO_3^{2-} were selected to simulate background interference. Ion concentrations used were 0, 50, 150, 350, and 500 mg/L and the dose was 60 mg/50 ml. The results were illustrated in Figure 8.

As shown in Figure 8, Sb(III) adsorption efficiency was all over 97% for all ions. It should be noted that the removal efficiency showed a relatively low decrease with increase in anion concentration. The order of decrease in removal efficiency was $Cl^- < NO_3^- < SO_4^{2-} < PO_4^{3-} < AsO_3^{2-} < CO_3^{2-}$. Actually, this phenomenon was related to the degree of association of above ions with soluble Sb species impacting on removal efficiency.

3.3. Adsorption Kinetics. In order to study the kinetics of Fe_3O_4/GO absorbing Sb(III), a series of Sb(III) solutions with concentration of 10 mg/L and initial pH value of 7.0 were taken and 60 mg of Fe_3O_4/GO was added to each solution. When temperature was 298 K, the variation of adsorption (q_t) with the change of time was measured. Pseudo-first-order kinetic model and pseudo-second-order kinetic model were adapted to analyze characteristics of adsorption kinetics. Model equations are listed as Formula (5) [18].

$$\ln\left(q_e - q_t\right) = \ln q_e - k_1 t,$$

$$\frac{t}{q_t} = \frac{1}{k_2 q_e^2} + \frac{1}{q_e} t, \tag{5}$$

where q_t and q_e (mg/g) are the amounts of Sb(III) adsorbed onto Fe_3O_4/GO at time t and at equilibrium, respectively; k_1 is the rate constant, determined by plotting $\ln(q_e - q_t)$ versus t; and k_2 is the rate constant.

For the first-order kinetic equation of specified initial concentration, $\ln(q_e - q_t)$ to time (t) was plotted, and the linear fitting was done. The first-order and second-order kinetics fit lines (Figure 9) were obtained by the fitted parameters. Similarly, for second-order kinetic equation, t/q_t to time was graphed and the linear fitting was undertaken. The second-order kinetics fit line in Figure 9 was based on the best fit parameters.

From Figure 9, it is clear that the adsorption of Sb(III) by Fe_3O_4/GO is more suitable for the pseudo-first-order kinetics model which implies a simple sorption mechanism rather than chemical reaction.

3.4. Adsorption Thermodynamics. In order to study the thermodynamic characteristics of Sb(III) adsorption by Fe_3O_4/GO, a series of Sb(III) solutions with various concentrations and initial pH value of 7.0 were taken. The solutions were put in constant temperature incubation box (298 K) and the adsorption was performed for 24 hours. The equilibrium absorption capacity (q_e) as a function of equilibrium concentration (C_e) at the different temperatures was plotted as the adsorption isotherms of Sb(III) in Figure 8.

Data were fitted using the Langmuir [21] and Freundlich [22] isotherm models, and the equations for both models are presented as Formula (6).

$$\frac{C_e}{q_e} = \frac{C_e}{q_{\max}} + \frac{1}{q_{\max} K_L},$$

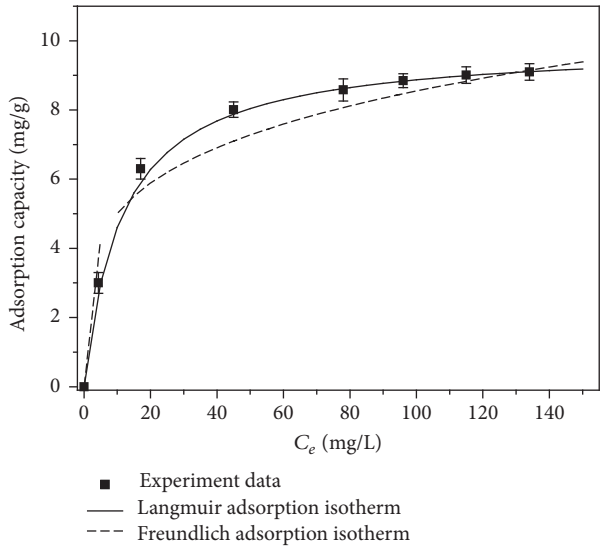

Figure 10: Thermodynamic models for fitting Sb(III) adsorption using Fe_3O_4/GO.

$$\ln q_e = \ln K_F + \frac{1}{n} \ln C_e, \tag{6}$$

where C_e is the mass concentration of Sb(III) when the solution is in the state of adsorption equilibrium; K_L is the Langmuir adsorption constant. K_F is a Freundlich constant related to adsorption capacity and $1/n$ is an empirical parameter giving an indication of the favorability of adsorption. It is conducted that when $1/n$ is between 0.1 and 0.5 the adsorbate is easily adsorbed, while when $1/n$ is larger than 2.0 it is difficult to adsorb [6].

From Figure 10, it can be seen that the adsorption reaction matches the Langmuir isothermal adsorption model, which indicated that the adsorption of Sb(III) onto Fe_3O_4/GO was the monolayer adsorption. Moreover, adsorbing capacity increased with an increase in temperature. Meanwhile, $0.1 < 1/n < 0.5$ in Table 1, which meant that the reaction was thermodynamically favourable.

Thermodynamic parameters were calculated by the formulas shown below [23]:

$$\Delta G = -RT \ln K_D, \tag{7}$$

$$\Delta G = \Delta H - T\Delta S, \tag{8}$$

$$\ln K_D = \frac{\Delta S}{R} - \frac{\Delta H}{RT}, \tag{9}$$

where K_D is the solid-liquid distribution coefficient [24]; ΔG is the Gibbs free energy change value in adsorption process, kJ/mol; ΔH is the caloric value in adsorption process, kJ/mol; ΔS is the entropy change value in adsorption, J/(mol·K).

Based on the experimental results of the adsorption of Sb(III) onto Fe_3O_4/GO, the linear imitation was graphed in Figure 11 $1/T$ was the abscissa while $\ln K_D$ was the ordinate. According to Formula (9) and the obtained slope and intercept of the straight line, ΔH and ΔS were calculated, and ΔG in the corresponding temperature was calculated by Formula (7). The results were presented in Table 2.

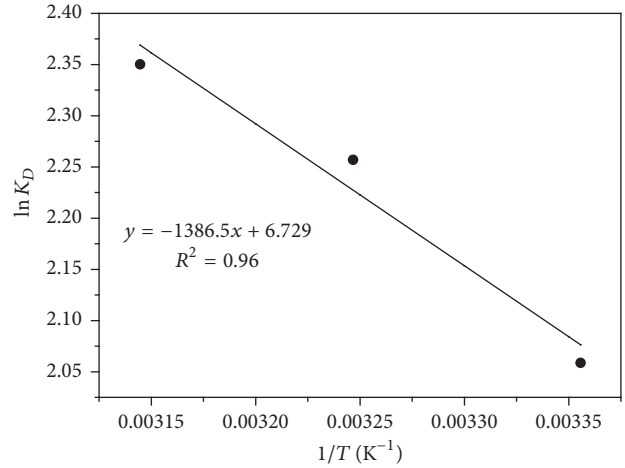

Figure 11: Thermodynamic parameters linear fit.

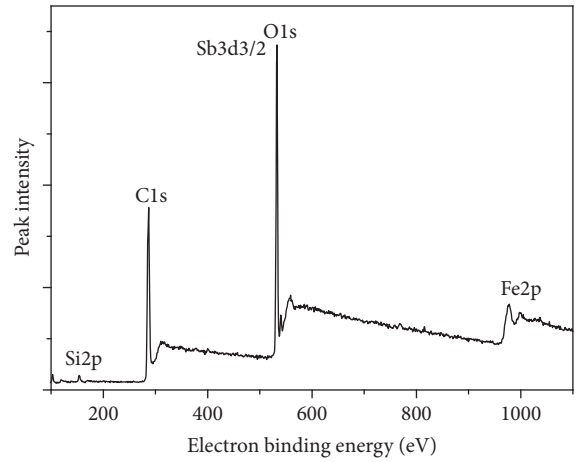

Figure 12: The total element distribution spectrum after adsorption Sb(III).

Table 2 showed that the adsorption reaction was a spontaneous process when the Gibbs free energy change value (ΔG) was below zero. And when $\Delta S > 0$, the adsorption process increased the entropy of the process. As for the ΔH, the adsorption reaction was an endothermic process when its value was over zero and thus the temperature rise was helpful to move the reaction forward.

3.5. Analysis of Adsorption Mechanism. The XPS results of Fe_3O_4/GO after the adsorption of Sb(III) were depicted in Figure 12. There was a peak of Sb in the spectrum, which coincided with the peak of O1s. The spectrum of Sb after adsorption was presented in Figure 14. The spectra of the surface oxygen of Fe_3O_4/GO (before and after adsorption) were shown in Figures 13 and 14, respectively.

The binding energies of Sb($3d_{5/2}$) and Sb($3d_{3/2}$) detected by XPS were 530.11 eV and 539.75 eV. According to the XPS

Table 1: The adsorption isothermal eq. parameters of Fe_3O_4/GO.

T (K)	$q_{e,\exp}$ (mg/g)	Langmuir adsorption isotherm			Freundlich adsorption isotherm		
		$q_{\max}$ (mg/g)	K_L (L/mg)	R^2	K_F	$1/n$	R^2
298	9.56	9.59	0.113	0.95	2.95	0.23	0.88

Table 2: The adsorption thermodynamic parameters of Sb(III) using Fe_3O_4/GO.

T (K)	ΔG (kJ/mol)	ΔH (kJ/mol)	ΔS (KJ/(mol·K))
298	−5.158		
308	−5.718	11.53	0.056
318	−6.278		

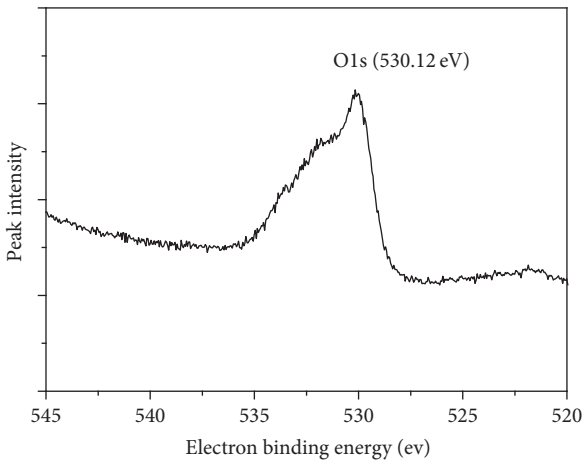

Figure 13: The spectrum of O1s before adsorption.

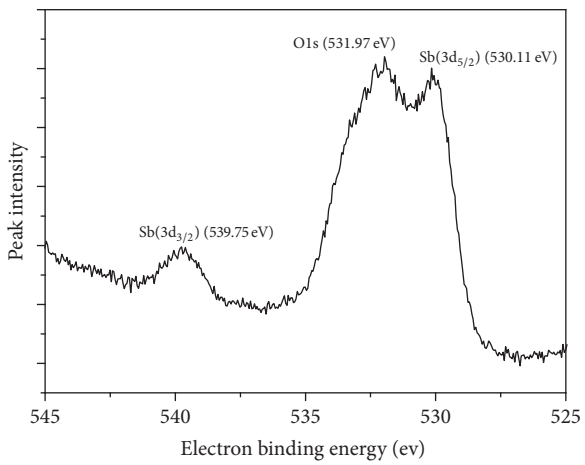

Figure 14: The spectrum of Sb3d and O1s after adsorption.

chemical state database, the superficial antimony on the Fe_3O_4/GO exists as Sb_2O_5, in which the antimony was pentavalent. However, the antimony of $K(SbO)C_4H_4O_6{\cdot}1/2H_2O$ used for preparing stock solutions was as a trivalent species. It demonstrated that the absorption process was accompanied with redox reaction, oxidizing the Sb III.

In order to further analyze the relation between bind energy displacement of O(1s) and surface charge, De Jong et al. [25] constructed a simplified mathematical model (10):

$$Q_o = -4.372 + \left[385.023 - 8.976 * \left(545.509 - X_{o(1s)}\right)\right] 1/2 \quad /4.488, \tag{10}$$

where Q_o is charge of oxygen atom (esu); $X_{o(1s)}$ is binding energy measured by XPS (eV).

The charge variation of oxygen atom before and after the adsorption of Sb(III) onto GO was calculated by Formula (10), and the results are presented in Table 3.

Table 3 shows the charge of oxygen atom was changed from −0.871/esu to −0.738/esu during the adsorption of antimony onto Fe_3O_4/GO. Therefore, it could be concluded that the outer electron of oxygen atom transferred and the density of electrons changed during the adsorption process demonstrating that redox reaction occurred during the adsorption process.

3.6. Adsorbent Reuse. Reusability is a key factor in the investigation of adsorbent performance. A 0.1 mol/L of ethylene diamine tetraacetic acid (EDTA) solution was utilized in this experiment as a useful chelating agent to enhance removal of strongly adsorbed Sb and test reusability of the sorbent. The results showed Fe_3O_4/GO lost 50% of its efficiency after five continuous adsorption-regeneration-adsorption cycles as an adsorbent. This degradation may be due to decomposition of the sorbent or blocking of exchange sites by the EDTA.

4. Conclusions

The magnetic adsorbent Fe_3O_4/GO was synthesized and was studied in the removal of antimony from solution. The rate of removal rate of antimony was greatest in the pH range of 3.0–9.0. Reaction kinetics indicated that the adsorption of antimony onto Fe_3O_4/GO followed a pseudo-first-order kinetic model. The adsorption of Sb(III) onto synthesized Fe_3O_4/GO matched a Langmuir isothermal adsorption model according to reaction thermodynamics and the maximum adsorption capacity was found to be 9.59 mg/g. The thermodynamic parameters of the adsorption proved that the adsorption of Sb(III) onto Fe_3O_4/GO was a spontaneous and endothermic process. The XPS before and after adsorption and the relation between the binding energy displacement of O(1s) and surface charge indicated that the adsorption process was accompanied by a redox reaction. In

Table 3: Binding energy, charge change, and electron transfer direction of the oxygen atom in the adsorption process.

	Binding energy/eV	Electric charge/esu	Oxygen electron transfer direction
Fe_3O_4/GO	530.12	−0.871	
Fe_3O_4/GO + Sb	532.25	−0.738	Provide electronic

addition, the regeneration test demonstrated that Fe_3O_4/GO composite has good reuse potential.

Conflicts of Interest

The authors declare that they have no conflicts of interest.

Acknowledgments

This work was financially supported by the National Natural Science Fund Project of Hunan Province (2016JJ6040) and the National Natural Science Foundation of China (51604113). The authors deeply appreciate this support.

References

[1] S. Sundar and J. Chakravarty, "Antimony toxicity," *International Journal of Environmental Research and Public Health*, vol. 7, no. 12, pp. 4267–4277, 2010.

[2] X. Yang, Z. Shi, M. Yuan, and L. Liu, "Adsorption of trivalent antimony from aqueous solution using graphene oxide: Kinetic and thermodynamic studies," *Journal of Chemical and Engineering Data*, vol. 60, no. 3, pp. 806–813, 2015.

[3] Council of the European Communities., "Council Directive 76/464/EEC of 4 may 1976 on pollution caused by certain dangerous substances discharged into the aquatic environment of the Community," *Official Journal L*, vol. 129, pp. 23–29, 1976.

[4] USEPA, *Water related fate of the 129 priority pollutants*, vol. 1, USEPA, Washington D.C., USA, 1979.

[5] M. Kang, T. Kamei, and Y. Magara, "Comparing polyaluminum chloride and ferric chloride for antimony removal," *Water Research*, vol. 37, no. 17, pp. 4171–4179, 2003.

[6] Y. Leng, W. Guo, S. Su, C. Yi, and L. Xing, "Removal of antimony(III) from aqueous solution by graphene as an adsorbent," *Chemical Engineering Journal*, vol. 211-212, pp. 406–411, 2012.

[7] United States Environmental Protection Agency, *Toxics Release Inventory*, USEPA, Washington DC, USA, 1998.

[8] C. G. Anderson, "The metallurgy of antimony," *Chemie der Erde - Geochemistry*, vol. 72, no. 4, pp. 3–8, 2012.

[9] Z. Wu, M. He, X. Guo, and R. Zhou, "Removal of antimony (III) and antimony (V) from drinking water by ferric chloride coagulation: Competing ion effect and the mechanism analysis," *Separation and Purification Technology*, vol. 76, no. 2, pp. 184–190, 2010.

[10] T. Gebel, "Aresnic and antimony: Comparative approach on mechanistic toxicology," *Chemico-Biological Interactions*, vol. 107, no. 3, pp. 131–144, 1997.

[11] K. Oorts, E. Smolders, F. Degryse et al., "Solubility and toxicity of antimony trioxide (Sb2O3) in soil," *Environmental Science and Technology*, vol. 42, no. 12, pp. 4378–4383, 2008.

[12] M. Filella, N. Belzile, and Y. Chen, "Antimony in the environment: a review focused on natural waters: I. Occurence," *Earth-Science Reviews*, vol. 57, no. 1-2, pp. 125–176, 2002.

[13] G. Zhao, J. Li, X. Ren, C. Chen, and X. Wang, "Few-layered graphene oxide nanosheets as superior sorbents for heavy metal ion pollution management," *Environmental Science and Technology*, vol. 45, no. 24, pp. 10454–10462, 2011.

[14] T. F. Jiao, Y. Z. Liu, Y. T. Wu et al., "Facile and scalable preparation of graphene oxide-based magnetic hybrids for fast and highly efficient removal of organic dyes," *Scientific Reports*, vol. 5, Article ID 12451, 2015.

[15] P. S. Teo, H. N. Lim, N. M. Huang, C. H. Chia, and I. Harrison, "Room temperature *in situ* chemical synthesis of Fe_3O_4/graphene," *Ceramics International*, vol. 38, no. 8, pp. 6411–6416, 2012.

[16] Y.-P. Chang, C.-L. Ren, J.-C. Qu, and X.-G. Chen, "Preparation and characterization of Fe_3O_4/graphene nanocomposite and investigation of its adsorption performance for aniline and *p*-chloroaniline," *Applied Surface Science*, vol. 261, pp. 504–509, 2012.

[17] X. Yang, Z. Shi, and L. Liu, "Adsorption of Sb(III) from aqueous solution by QFGO particles in batch and fixed-bed systems," *Chemical Engineering Journal*, vol. 260, pp. 444–453, 2015.

[18] P. Zong, S. Wang, Y. Zhao, H. Wang, H. Pan, and C. He, "Synthesis and application of magnetic graphene/iron oxides composite for the removal of U(VI) from aqueous solutions," *Chemical Engineering Journal*, vol. 220, pp. 45–52, 2013.

[19] Y. Hao, Z. Wang, J. Gou, and Z. Wang, "Kinetics and thermodynamics of diquat removal from water using magnetic graphene oxide nanocomposite," *Canadian Journal of Chemical Engineering*, vol. 93, no. 10, pp. 1713–1720, 2015.

[20] M. Kang, M. Kawasaki, S. Tamada, T. Kamei, and Y. Magara, "Effect of pH on the removal of arsenic and antimony using reverse osmosis membranes," *Desalination*, vol. 131, no. 1-3, pp. 293–298, 2000.

[21] I. Langmuir, "The adsorption of gases on plane surfaces of glass, mica and platinum," *The Journal of the American Chemical Society*, vol. 40, no. 9, pp. 1361–1403, 1918.

[22] H. M. F. Freundlich, "Uber die adsorption in lusungen," *The Journal of Physical Chemistry*, vol. 57, pp. 385–470, 1906.

[23] A. Sari, D. Çitak, and M. Tuzen, "Equilibrium, thermodynamic and kinetic studies on adsorption of Sb(III) from aqueous solution using low-cost natural diatomite," *Chemical Engineering Journal*, vol. 162, no. 2, pp. 521–527, 2010.

[24] J. Xi, M. He, and C. Lin, "Adsorption of antimony(III) and antimony(V) on bentonite: Kinetics, thermodynamics and anion competition," *Microchemical Journal*, vol. 97, no. 1, pp. 85–91, 2011.

[25] B. H. W. S. De Jong, D. Ellerbroek, and A. L. Spek, "Low-temperature structure of lithium nesosilicate, Li_4SiO_4, and its Li1s and O1s X-ray photoelectron spectrum," *Acta Crystallographica Section B*, vol. 50, no. 5, pp. 511–518, 1994.